Journal of Zhejiang University-SCIENCE A 2026 27(2):142-154
www.jzus.zju.edu.cn; www.springer.com/journal/11582
E-mail: jzus_a@zju.edu.cn

Research Article

https://doi.org/10.1631/jzus.A2500436

Numerical investigation of the flow pattern around a vertical cylinder under wave action

Ben HE[1], Junkang WENG[2], Yuan LIN[2], Yifan GAO[1], Maoxing WEI[2], Fang HE[2]✉

[1]*PowerChina Huadong Engineering Co., Ltd., Hangzhou 311100, China*
[2]*Ocean College, Zhejiang University, Zhoushan 316021, China*

Abstract: The interaction between vertical cylinders and waves is an important research problem due to the prevalence of cylinder-type structures in marine infrastructure. A major goal is to improve their design for greater stability in the presence of waves. In this study, we numerically investigate the formation of vortices around a vertical cylinder under wave action, emphasizing the role of the flow field in potential bed erosion. Surface pressure distribution analysis elucidates the generation and evolution of the vortices, while the spatial distributions of bed shear stress quantify the significant influence of the flow field and vortex dynamics on scour around the cylinder. Numerical simulations were performed over a range of Keulegan-Carpenter (KC) numbers (12–26) to systematically resolve the 3D flow structures. Validation against particle image velocimetry (PIV) data confirms the accuracy of these simulations. Our results show that both the strength and spatial extent of the horseshoe vortex increase markedly with increasing KC number, leading to intensified bed shear stress and elevated scour potential around the cylinder.

Key words: Horseshoe vortex; Pressure distribution; Keulegan-Carpenter (KC) number; Vortex strength; Bed shear stress

1 Introduction

The response of vertical cylindrical structures to wave action has garnered increasing attention due to the prevalence of cylinder-type structures in ocean engineering (Chanda et al., 2022; Sarkar and Chanda, 2022; Guan et al., 2024). This is a critical area of study in coastal and offshore engineering, with direct implications for the design and stability of marine infrastructure, including bridge piers, offshore wind turbine foundations, and oil and gas platforms (Blondeaux, 2012; Qi et al., 2019). Under wave action, these structures are subjected to complex flow dynamics, in particular the formation of coherent vortices, i.e., the horseshoe vortex, which significantly influences local scour processes. Scouring around cylindrical foundations remains a primary cause of structural failure. Although many experiments have empirically quantified scour depth, few have examined the underlying flow mechanisms that drive sediment transport.

In steady currents, it is well understood that the horseshoe vortex and lee-wake vortex formed at the windward and leeward sides of the cylinder represent the two primary coherent structures (Qi and Gao, 2014; Schanderl et al., 2017; Qi et al., 2022). Laursen and Toch (1956) demonstrated that cylindrical obstructions cause flow deceleration and create an adverse pressure gradient, which promotes boundary layer separation and leads to the formation of a horseshoe vortex. Early investigations by Berger and Wille (1972) into the lee-wake vortex generated by the flow around a cylinder in a unidirectional flow field analyzed the variational trends of this vortex as caused by changes in the Reynolds number (*Re*). Their research identified two modes of lee-wake vortex behavior at low Reynolds numbers: a low-speed mode within the range $40<Re<110$, and a high-speed mode within $80<Re<160$. Two distinct modes were identified within the turbulent horseshoe vortex system region: the back-flow mode and the zero-flow mode. The back-flow mode features a pronounced near-wall jet flowing against the mainstream direction. In contrast, the zero-flow mode occurs when the

---

✉ Fang HE, hefang@zju.edu.cn
Fang HE, https://orcid.org/0000-0002-5559-6230

Received Sept. 10, 2025; Revision accepted Oct. 11, 2025;
Crosschecked Dec. 5, 2025; Online first Jan. 6, 2026

incoming flow obstructs reversed fluid motion, triggering vertical ejection of the return flow (Devenport and Simpson, 1990). In addition to these two modes, Apsilidis et al. (2015) identified a new flow pattern, referred to as the intermediate mode, which indicated that the switching between the back-flow and zero-flow modes is discontinuous. Chen et al. (2017) employed particle image velocimetry (PIV) to measure the velocity fields in the upstream symmetry plane of the cylinder, investigating the dynamics of the turbulent horseshoe vortex. They showed that the turbulent horseshoe vortex system is governed by interactions between the back-flow, intermediate, and zero-flow modes.

Moreover, under wave action, horseshoe and lee-wake vortices may form periodically on either side of the cylinder (Jang et al., 2021). A key dimensionless parameter governing the formation of these vortices is the Keulegan-Carpenter (KC) number (Sumer et al., 1992). It is defined as $u_\mathrm{m}T/D$, where u_m is the maximum value of the undisturbed orbital velocity at the bed, T is the wave period, and D is the diameter of the cylinder. The experiments by Sumer et al. (1997) established critical thresholds for vortex dynamics around cylinders under wave conditions, and indicated that horseshoe vortex formation requires a KC number exceeding 6. With advancements in flow visualization methods, the horseshoe vortex structure around a cylinder has been captured experimentally (Bělík, 1973; Baker, 1980; Pierce and Harsh, 1988). Jang et al. (2021) conducted a numerical study to investigate the fields of oscillatory flow passing a vertical wall-mounted cylinder for varying KC numbers to understand the flow mechanisms around a cylinder in wave conditions. Moreover, He et al. (2024) employed time-resolved PIV to examine the characteristics of a horseshoe vortex, demonstrating that its strength is closely correlated with wave phase, initially decreasing and then increasing within a wave period.

Compared to the extensive studies on flow field characteristics in steady flows, there is a lack of systematic research on the evolution mechanism of the flow field around a cylinder under wave action and the development of vortex structures. In particular, the influence mechanism of flow field characteristics and vortex structure evolution on scour remains unclear. Therefore, the present study addresses this gap. Using experiment-validated computational fluid dynamics (CFD), we conduct simulations across seven KC conditions to examine the temporal evolution of flow field structures around a cylinder subjected to wave action. Accordingly, the following results are provided: (i) phase-resolved, 3D descriptions of horseshoe and lee-side vortex evolution, (ii) an analysis of the localized flow features (impinging jets, corner separation, and vortex breakdown) that produce transient peaks in bed shear stress, and (iii) mechanistic links that connect these flow features to short-term sediment entrainment potential.

2 Numerical setup

2.1 Governing equations and boundary conditions

All numerical calculations in this study are based on the Reynolds-averaged Navier-Stokes (RANS) equations, which are employed to strike a balance between computational efficiency and solution accuracy. Turbulence is modeled using the shear stress transport (SST) k-ω model. The mass and momentum conservation equations are discretized using the finite-volume method (FVM) and are solved with the semi-implicit method for pressure-linked equations-consistent (SIMPLEC) algorithm for pressure-velocity coupling. The convergence criteria are monitored during iterative computations to obtain the pressure and velocity fields. The free surface is represented using the volume of fluid (VOF) method.

A 3D numerical wave flume is constructed with a Cartesian coordinate system, where the x-axis aligns with the direction of wave propagation, the y-axis represents the transverse width of the flume, and the z-axis is orthogonal to the still water free surface (indicating the water depth direction). The vertical cylinder is positioned in the center of the x-y plane, and the velocity components along the x, y, and z axes are denoted as u, v, and w, respectively. The computational domain extends over: $-4.5L<x<4.5L$ (where L is the wavelength), $-0.2\ \mathrm{m}<y<0.2\ \mathrm{m}$, and $0<z<h+2H$ (with h representing the water depth, and H indicating the wave height).

In terms of the boundary conditions, the velocity inlet method is adopted for wave generation: the left boundary ($x=-4.5L$) is set as the velocity inlet for inputting wave signals. The right boundary ($x=4.5L$) was specified as a pressure outlet. To avoid spurious wave reflections at this boundary, the pressure outlet is preceded by a wave-damping zone in which an explicit momentum sink is applied to the vertical velocity component. The sink follows the commonly used Choi and Yoon (2009) damping approach (i.e., a momentum source term added to the vertical momentum equation). The bottom (z=0) is modeled as a no-slip wall; the top surface ($z=h+2H$) is a pressure outlet; both side surfaces ($y=\pm0.2$ m) are set as symmetry planes. Schematic diagram for the simulation domain is shown in Fig. 1.

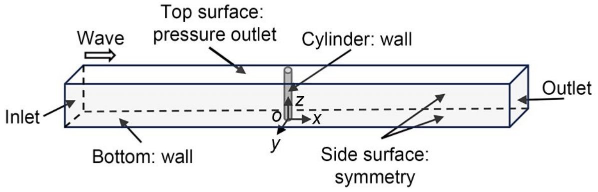

Fig. 1 Schematic diagram for the simulation domain showing the boundary conditions

2.2 Mesh generation and grid sensitivity

A trimmed grid approach is employed to achieve a balance between numerical simulation accuracy and computational efficiency. The baseline grid size is set at 0.4 m, with a surface growth rate of 1.5 applied to the boundary surfaces. Five layers of boundary grids are established to resolve the boundary layer. Through iterative calculations, the total thickness of the boundary layer is set to be 0.5 times the minimum grid size, thus ensuring that the height of the first grid layer near the wall satisfies the turbulent simulation requirement that $y^+\approx1$. Both volume and surface grids employ a slow growth rate mode, allowing a smooth transition from the wall region to the far field. This approach ensures precise modeling of the velocity gradient characteristics within the boundary layer while avoiding numerical dissipation issues caused by grid distortion. For the cutting body in the water tank, the anisotropic grid sizes are defined as follows: 0.10 m in the x-direction, 0.10 m in the y-direction, and 0.05 m in the z-direction. To analyze wave height and wavelength accurately, the grids near the free surface ($h-H<z<h+H$) are refined. Mesh distribution is shown in Fig. 2.

To ensure mesh independence, three mesh sizes were tested, as detailed in Table 1. The model was validated using a fifth-order Stokes regular wave with a period of 1.8 s, a height of 10 cm, and a water depth of 30 cm. The results are presented in Table 2. For computational efficiency, Mesh 1 was adopted for the simulations in this study.

The primary objective of this study is to investigate the characteristics of the flow field around a cylinder subjected to wave action. To ensure accurate simulations, refining the local mesh near the cylinder is critical. There are three main aspects to the mesh refinement: (i) Control the mesh size on the cylindrical surface to $D/20$. (ii) Perform preliminary refinement of the flow field around the cylinder within the domain ($-D/2-H/2<x<D/2+H/2$, $-H/2<y<H/2$, $0<z<h-H$), where the mesh sizes in the x-, y-, and z-directions are $H/20$ each. (iii) Refine the critical horseshoe vortex region, with the mesh unit size in the x-direction being 1.2×10^{-3} m, in the y-direction being $H/20$, and in the z-direction being 1.2×10^{-3} m.

2.3 Model validation

To validate the numerical model, we compared simulated and experimental velocity profiles extracted above the bed at two vertical locations in the x-z plane, z=0.6 and 0.8 cm (corresponding to z/D=0.200 and 0.267, at t/T=0.41 (t is the time instant in the period), using time-resolved PIV data from He et al. (2024). Each profile was obtained by sampling the instantaneous velocity along a one-dimensional line in the x-direction at the PIV plane. For the simulation data, the

Table 1 List of simulations conducted for the grid sensitivity test

Grid scheme	Grid scale			Number of computational cells
	x direction (m)	y direction (m)	z direction (m)	
Mesh 1	$L/100$	0.05	$H/15$	2.1×10^5
Mesh 2	$L/120$	0.05	$H/20$	4.0×10^5
Mesh 3	$L/140$	0.05	$H/25$	7.9×10^5

Table 2 Results of the grid sensitivity test

Grid scheme	Crest average value	Crest theoretical value	Trough average value	Trough theoretical value	Error
Mesh 1	0.3657	0.3657	0.2667	0.2655	1.20%
Mesh 2	0.3652	0.3657	0.2666	0.2655	1.66%
Mesh 3	0.3655	0.3657	0.2668	0.2655	1.44%

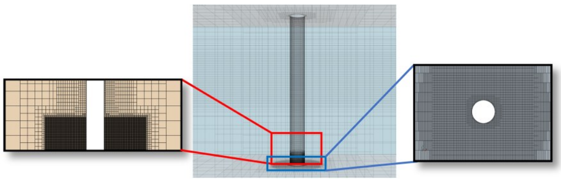

Fig. 2 Mesh distribution in the surroundings of the cylinder

velocity field was interpolated onto the experimental PIV plane and sampled at the same *x*-coordinates, ensuring collocated comparisons between the simulation and PIV data.

The selected heights sample the lower boundary layer and the vicinity of the horseshoe vortex (HSV) and are therefore representative for assessments of the model's capability to reproduce vortex-driven flow features. The numerical results are in good agreement with the PIV measurements at these heights, confirming that the model accurately reproduces both the magnitude and phase-dependence of the velocity field in the vortex region. Comparisons of the results are presented in Section S1 of the electronic supplementary materials (ESM).

2.4 Test condition setup

The test conditions are provided in Table 3. In all tested cases, the water depth (h=0.40 m) and the diameter of the cylinder (D=0.03 m) were held constant. By varying the wave height (H) and period (T), a range of KC numbers was achieved.

Table 3 Test conditions

Case	h (m)	D (m)	H (m)	T (s)	KC number
1	0.40	0.03	0.10	1.8	12.36
2	0.40	0.03	0.10	2.2	16.12
3	0.40	0.03	0.10	2.4	17.94
4	0.40	0.03	0.10	2.6	19.74
5	0.40	0.03	0.12	2.4	21.53
6	0.40	0.03	0.12	2.6	23.69
7	0.40	0.03	0.16	2.2	25.79

3 Results and discussion

3.1 Streamlines and velocity distribution

In this section, representative cases (Cases 1, 3, 5, and 7) are selected to examine the effect of the KC number on the flow field. To eliminate the influence of physical dimensions and enable a unified quantitative comparison across multiple cases, the velocity is normalized by the maximum orbital velocity V/u_m (V is the velocity of wave particle).

Fig. 3 displays the streamlines and velocity distributions upstream of the cylinder for the selected cases. At t/T=0.36 (Fig. 3a), flow separation occurs upstream of the cylinder due to the adverse pressure gradient, leading to the formation of a distinct horseshoe vortex structure near the cylinder. The streamlines around the core of the vortex exhibit a regular rotational pattern, indicating a stable vortex structure with a significant influence on the surrounding flow. At t/T=0.41 (Fig. 3e), the intensity of the first horseshoe vortex gradually weakens. Within the region outlined by the red rectangle, an immature vortex structure emerges, where the streamlines display an open spiral pattern, and no clear vortex core is identified. Observing Fig. 3i, the previously incomplete vortex has now developed into a complete vortex structure at this moment. The streamlines in the flow field display a relatively regular rotational form around the vortex core, demonstrating stable spatial characteristics. At t/T=0.44, as shown in Fig. 3m, the strong vertical velocity gradient caused by the downward flow promotes the full development of the second horseshoe vortex, which spatially expands considerably.

As shown in Fig. 3b, at t/T=0.36, no obvious vortex structure has formed in the flow field in Case 3, which stands in contrast to Case 1. At t/T=0.41 (Fig. 3f), a distinct vortex core (outlined by the red rectangle) begins to appear near the cylinder. Interestingly, at t/T=0.44, Fig. 3n shows that two distinct vortices appear in the flow field in Case 3. The vortex core of the first vortex (marked by the red rectangle) is still located near the cylinder, while the vortex center of the second vortex (marked by the black rectangle) is at x/D=−3.0 and z/D=0.046. The emergence of a multi-vortex configuration indicates that waves may have a more intense scouring effect around the cylinder under such conditions.

Unlike in Case 3, no multiple vortices are observed in Case 5, where the horseshoe vortex remains localized near the cylinder. As depicted in Fig. 3o, the emergence of large-scale curved spiral streamlines suggests that the influence range of the horseshoe vortex expands progressively with increasing KC number, thereby intensifying the scouring effect. Compared to

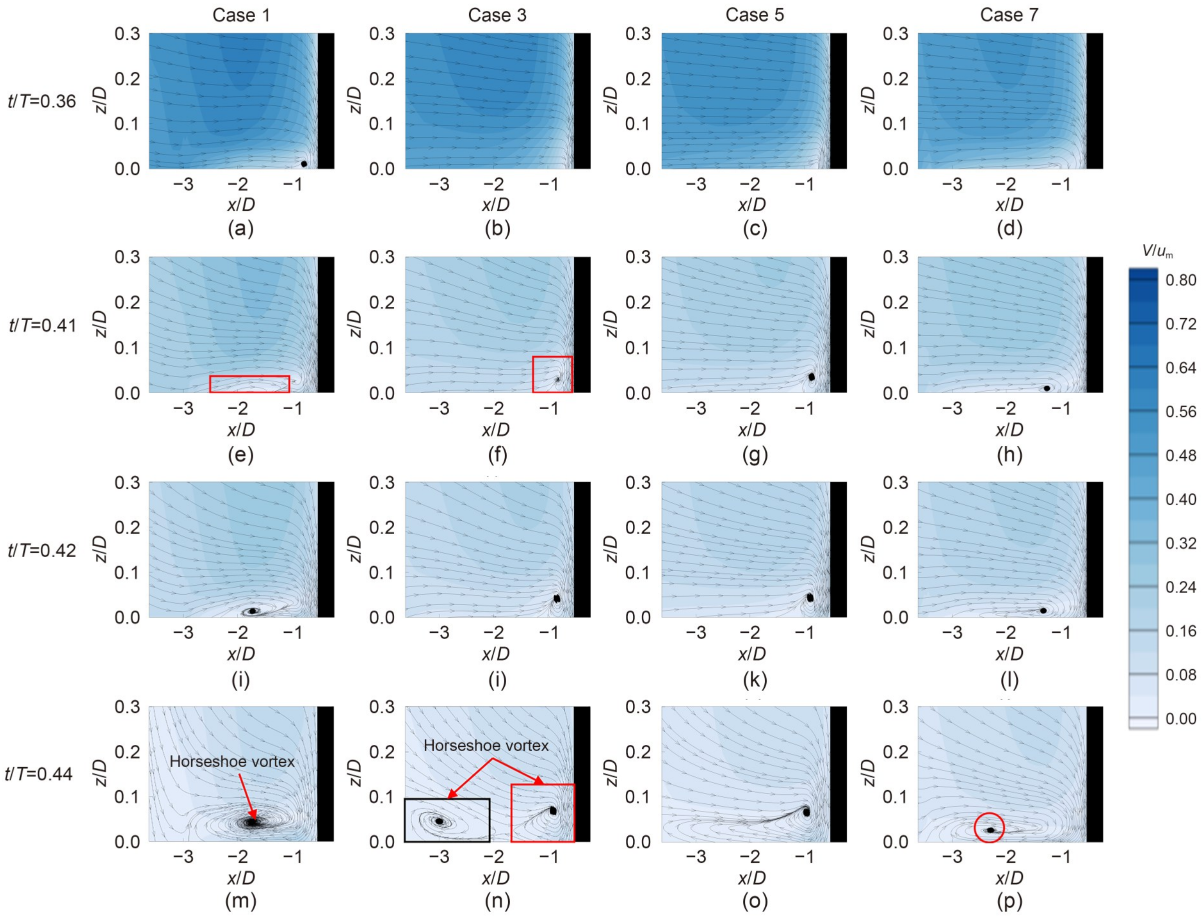

Fig. 3 Streamlines and velocity distributions in front of the cylinder: (a) Case 1 at t/T=0.36; (b) Case 3 at t/T=0.36; (c) Case 5 at t/T=0.36; (d) Case 7 at t/T=0.36; (e) Case 1 at t/T=0.41; (f) Case 3 at t/T=0.41; (g) Case 5 at t/T=0.41; (h) Case 7 at t/T=0.41; (i) Case 1 at t/T=0.42; (j) Case 3 at t/T=0.42; (k) Case 5 at t/T=0.42; (l) Case 7 at t/T=0.42; (m) Case 1 at t/T=0.44; (n) Case 3 at t/T=0.44; (o) Case 5 at t/T=0.44; (p) Case 7 at t/T=0.44. References to color refer to the online version of this figure

the situations in the previous cases, where the vortex core positions remained largely unchanged, in Case 7, as shown in Fig. 3p, the vortex core (outlined by the red circle) of the horseshoe vortex gradually moves away from the cylinder.

A discussion on the wake streamline and velocity distribution of the cylinder can be found in Section S2 of the ESM.

3.2 Analyses of vortex strength

The vortex intensity is quantified using the swirling strength (λ_{ci}), which is defined as the imaginary part of the complex root of the velocity gradient tensor (Zhou et al., 1999). Since the swirling strength reaches its maximum at the vortex center and decreases moving radially outward (Chen et al., 2019), it serves as a robust indicator of vortex intensity; this effectively mitigates the misidentification issues inherent in traditional vorticity-based methods. Vortex identification is performed using the region growing algorithm (Gao et al., 2011). Once the vortex area is identified, its strength is quantified by calculating the circulation Γ, via integration of the vorticity over the vortex's cross-sectional area that is bounded by the vortex boundary (Kolář, 2010):

$$\Gamma=\oint V\mathrm{d}C=\iint \omega\mathrm{d}S, \tag{1}$$

where V is the tangential velocity component along the vortex boundary C, and ω is the vorticity over the vortex cross section S bounded by C.

Fig. 4 shows the temporal evolution of vortex strength in front of the cylinder for each case. Between t/T=0.1 and 0.3, the vortex strength reaches its peak, which corresponds to the forward flow acceleration

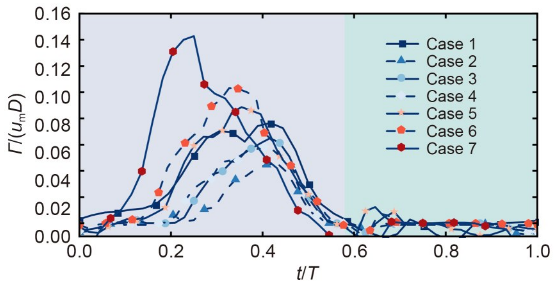

Fig. 4 Vortex strength in front of the cylinder for each case. References to color refer to the online version of this figure

phase. During this period, the boundary layer separation in front of the cylinder forms a strong shear layer, and the horseshoe vortex reaches the maximum activity. Notably, the peak vortex strength shows a systematic enhancement with increasing KC number, indicating stronger vortex energy and greater scouring potential at higher KC numbers. A marked decline in vortex strength occurs between *t*/*T*=0.4 and 0.6, which is the flow reversal phase. These two phases correspond to the gray background regions in the figure, and represent active horseshoe vortex development upstream of the cylinder, where there are relatively high values for all cases.

At *t*/*T*=0.6, the horseshoe vortex is significantly weakened as the flow reverses and energy dissipates into turbulent kinetic energy. The subsequent phase (*t*/*T*=0.8–1.0) is characterized by low vortex strength, indicating minimal activity of the horseshoe vortex. This stage is indicated by the green background regions in the figure. During this period, the upstream side of the cylinder is the leeward side. Thus, there are almost no horseshoe vortices.

Although the overall trend of vortex strength evolution is consistent across different cases, differences in peak intensity are observed. As shown in Fig. 4, higher KC numbers generally yield greater vortex intensities, with Case 7 (the case with the highest KC number) showing an advanced phase of peak occurrence. This suggests KC-dependent changes to the vortex dynamics. However, an anomaly is noted where Case 1 (the case with the lowest KC number) exhibits a higher intensity than Cases 2 and 3. As shown in Fig. 3a, Case 1 (low KC number) displays a relatively large, compact vortex region whose core remains coherent and comparatively un-twisted; consequently, integrated metrics that sum the rotation over the coherent region give a higher value than for Cases 2 and 3, in which the flow has stronger shear and shows vortex splitting. In other words, Case 1 produces a larger, less fragmented coherent vortex at this phase, so integrated measures of its vortex intensity can exceed those of higher-KC cases, even when the local peak vorticity is smaller. In other cases, the increasing KC trend (higher vortex intensity for larger KC number) reappears.

3.3 Evolution of vortex structures

To further quantify the characteristics of the vortices around the cylinder, Figs. 5 and 6 show contour maps of the *Q* criterion at selected phases, in which *Q* is calculated as:

$$Q=\frac{1}{2}\left(\|\boldsymbol{\Omega}\|^2-\|\boldsymbol{S}\|^2\right), \tag{2}$$

where $\boldsymbol{\Omega}$ is the antisymmetric tensor, and $\boldsymbol{S}$ is the symmetric tensor.

$$\boldsymbol{\Omega}=\frac{1}{2}(\nabla\boldsymbol{v}-\nabla\boldsymbol{v}^{\mathrm{T}}), \tag{3}$$

$$\boldsymbol{S}=\frac{1}{2}(\nabla\boldsymbol{v}+\nabla\boldsymbol{v}^{\mathrm{T}}), \tag{4}$$

where $\nabla\boldsymbol{v}$ is the velocity gradient tensor.

To more effectively capture the evolution of vortex structures within the flow field, a threshold value of Q=100 s^{-2} was determined from comprehensive validation across all relevant cases. As shown in Fig. 5a, in Case 1, at *t*/*T*=0.24, the horseshoe vortex begins to form

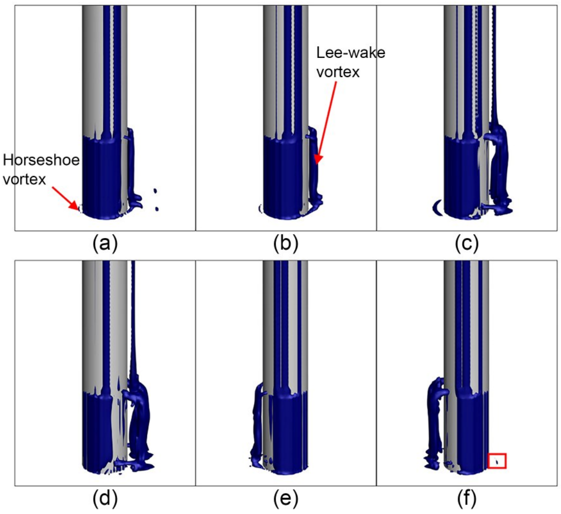

Fig. 5 *Q* criterion contour around the cylinder at different phases in Case 1: (a) *t*/*T*=0.24; (b) *t*/*T*=0.26; (c) *t*/*T*=0.39; (d) *t*/*T*=0.45; (e) *t*/*T*=0.74; (f) *t*/*T*=0.88. References to color refer to the online version of this figure

upstream of the cylinder and develops in a clockwise direction around the cylinder. At t/T=0.39 (Fig. 5c), the horseshoe vortex evolves more and tends to move away from the cylinder, covering about one-quarter of the cylinder's circumference. Its topology displays a characteristic Ω-shaped structure. The vortex persists until t/T=0.45 (Fig. 5d), during which the horseshoe vortex contracts and dissipates, rather than rupturing. Starting from t/T=0.26 (Fig. 5b), the lee-wake vortex emerges downstream of the cylinder. At t/T=0.39 (Fig. 5c), the lee-wake vortex begins to shed; this shedding occurs when the vortex reaches a critical size, at which point the balance between centrifugal force and pressure gradient is disrupted, causing the vortex to detach from the cylinder's surface. When t/T=0.74, the flow begins to reverse. Notably, the duration of the downstream horseshoe vortex is much shorter compared to its upstream counterpart, only emerging at t/T=0.88 (Fig. 5f, marked by a red box). Its spatial extent is also significantly smaller than that of the upstream horseshoe vortex.

As shown in Fig. 6a, in Case 7 at t/T=0.15, the upstream horseshoe vortex begins to form and continues to move away from the cylinder in the subsequent development, migrating upstream until it dissipates at t/T=0.38. When t/T=0.30, the lee-wake vortex starts to develop, and a large area of the vortex region (outlined by a red rectangle) is observed near the bed. This phenomenon is likely a result of the upstream horseshoe vortex being deflected downstream by the flow. It moves around both sides of the cylinder and eventually reaches the downstream region. The interaction between this vortex and the lee-wake vortex leads to the formation of a vortex tube structure, as illustrated in Fig. 6b. Under loose bed conditions, this structure would entrain sediment from the bed and continuously transport it downstream of the cylinder, causing scour to occur upstream of the cylinder. This mechanism may explain why scour is more pronounced at higher KC numbers. After flow reversal, the downstream horseshoe vortex becomes more prominent compared to Case 1 (Fig. 6d), persisting until t/T=0.95. This indicates that for high KC numbers, the downstream horseshoe vortex exhibits greater stability, maintaining its structure and characteristics for a longer period.

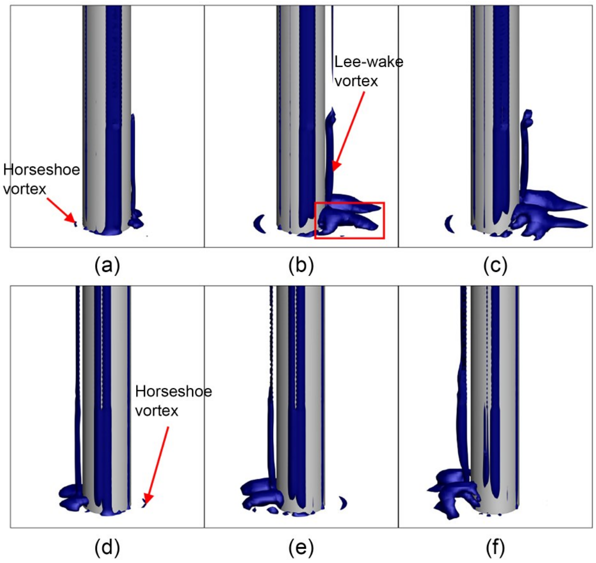

Fig. 6 ***Q* criterion contour around the cylinder at different phases in Case 7: (a) *t*/*T*=0.15; (b) *t*/*T*=0.30; (c) *t*/*T*=0.38; (d) *t*/*T*=0.74; (e) *t*/*T*=0.84; (f) *t*/*T*=0.95. References to color refer to the online version of this figure**

3.4 Pressure distribution

This section presents a comparative analysis of the pressure distribution and associated pressure gradients along the cylinder surface for Case 7. All pressure values P discussed herein refer to the atmospheric pressure; hence, it is null at the water surface. The dynamic pressure P_d is derived from the difference between the total pressure P and the hydrostatic pressure P_h, and is calculated as:

$$P_\mathrm{d}=P-P_\mathrm{h}=P-\rho g h_i, \tag{5}$$

where ρ is the density of water, g is the gravitational acceleration, and h_i is the vertical distance from the point to the water surface.

To better characterize the pressure distribution along the cylinder surface, a central angle φ is defined in the x-y plane with the vertical cylinder axis as the origin, where the clockwise direction is designated as positive. This is illustrated in Fig. 7.

Figs. 8 and 9 illustrate the distribution characteristics of total pressure P and dynamic pressure P_d along the z-axis at the front (φ=0°) and rear (φ=180°) of the cylinder, respectively. The dynamic pressure distribution is a key factor influencing flow separation behavior. Its asymmetry relative to the vertical plane (y-z plane) generates horizontal forces on the cylinder acting along the x-axis, making it critical for understanding flow field dynamics and vortex formation mechanisms. At t/T=0.125, the dynamic pressure P_d on the windward side (φ=0°) significantly exceeds the pressure

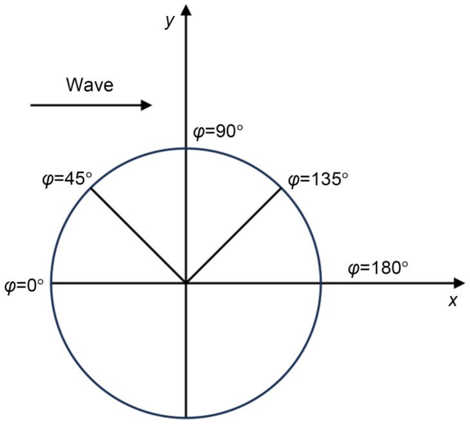

Fig. 7 Diagram of the central angle φ in the x-y plane

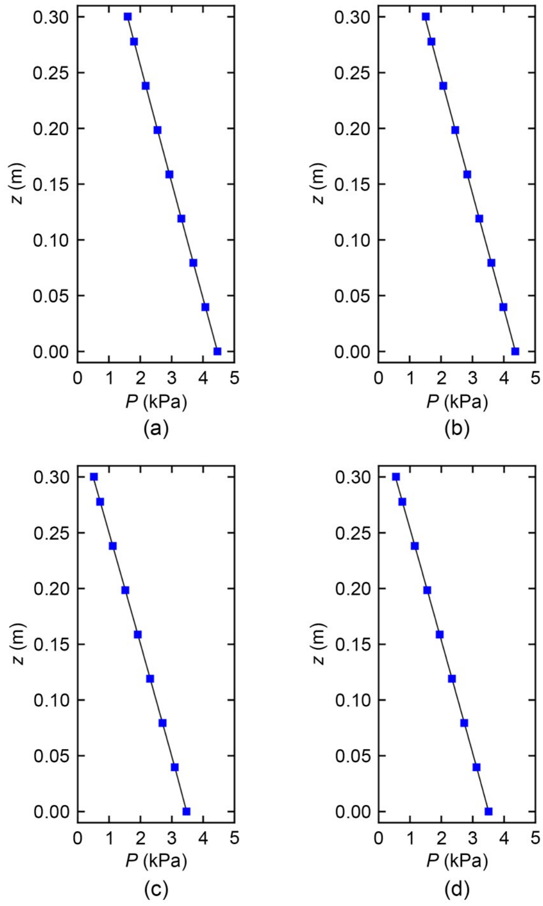

Fig. 8 Vertical distribution of total pressure P: (a) t/T=0.125, φ=0°; (b) t/T=0.125, φ=180°; (c) t/T=0.875, φ=0°; (d) t/T=0.875, φ=180°

on the leeward side (φ=180°), resulting in a net horizontal force directed along the positive x-axis. Conversely, at t/T=0.875, the dynamic pressure exhibits front-back symmetry, which significantly reduces the magnitude of the horizontal force.

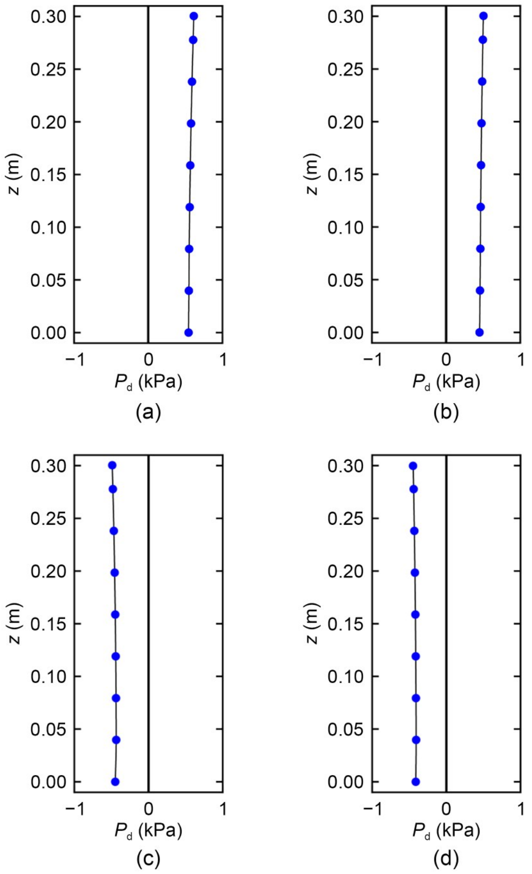

Fig. 9 Vertical distribution of dynamic pressure P_d: (a) t/T=0.125, φ=0°; (b) t/T=0.125, φ=180°; (c) t/T=0.875, φ=0°; (d) t/T=0.875, φ=180°

Dynamic pressure measurements around the cylinder further confirm that pressure variations at specific phases trigger flow separation within the boundary layers, ultimately initiating vortex shedding. Fig. 10 presents a plan view (x-y plane) of the dynamic pressure P_d distribution around the cylinder at z/D=0.1, where P_d is normalized by the density ρ of water and the maximum orbital velocity u_m (Corvaro et al., 2019). The pressure gradients around the cylinder, $\partial P/\partial S$ (where S is the length of the arc along the cylinder circumference), are analyzed to reveal their effect on flow dynamics. To better illustrate the pressure gradient differences among the various graphs, the plotting scales on Figs. 10a–10d differ. At t/T=0.125, a favorable pressure gradient ($\partial P/\partial S<0$) is observed within the range of $0°<\varphi<135°$, indicating a decrease in dynamic pressure along the positive x-axis. This gradient facilitates the transport of the horseshoe vortices generated in front of the cylinder–a phenomenon which was experimentally observed in mobile-bed experiments (Corvaro et al., 2018; Miozzi

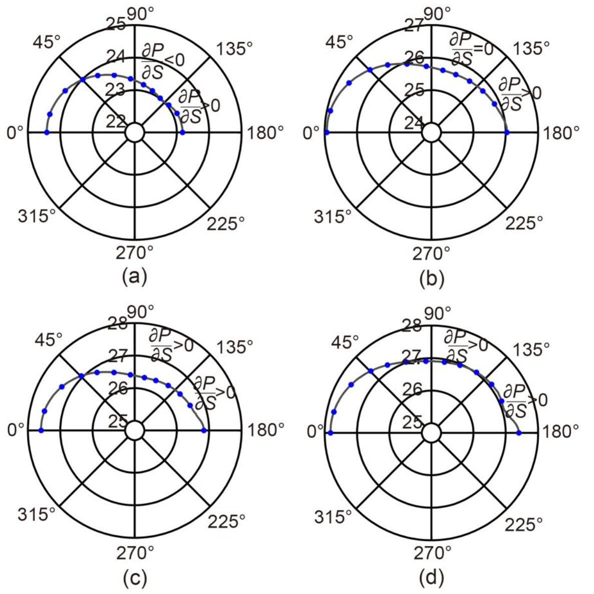

Fig. 10 Plan view (*x*-*y* plane) of the dynamic pressure distribution around the cylinder at different phases $\left(\frac{P_{\mathrm{d}}}{0.5\rho u_{\mathrm{m}}^2}\right)$: (a) *t*/*T*=0.125; (b) *t*/*T*=0.175; (c) *t*/*T*=0.20; (d) *t*/*T*=0.25

et al., 2019). On the other hand, a localized adverse pressure gradient ($\partial P/\partial S>0$) is observed in the range of 135°<φ<180°. As shown in Figs. 10b–10d, the region of adverse pressure gradient gradually expands (90°<φ<180°), promoting flow separation within the boundary layer and triggering the formation of the lee-wake vortex; this is one of the critical mechanisms in wave-induced scour.

3.5 Analyses of bed shear stress

Bed shear stress is a critical parameter determining sediment transport, since the instantaneous evolution of the horseshoe vortex directly leads to significant fluctuations in the instantaneous bed surface shear stress, thereby driving sediment mobilization (Dargahi, 1989; Li et al., 2018). Around the cylinder, instantaneous bed shear stress can be amplified by a factor of up to 10, highlighting the substantial impact of the flow field on sediment transport (Schanderl and Manhart, 2016). In this section, bed shear stress derived from numerical simulations is analyzed to assess the impact of the flow field on the overall bed shear stress distribution, as well as its implications for sediment transport and scour processes.

In the *x*-*z* plane (*y*=0), the influence of the horseshoe vortex on bed shear stress primarily manifests as an increase in the shear stress τ_x in the flow direction (*x*-direction), thereby driving downstream sediment transport. Based on the earlier discussion, the horseshoe vortex is predominantly active upstream of the cylinder, within the approximate range of $-3.0<x/D<-0.5$. In this range, we analyze the instantaneous bed shear stress τ_x over a period for Cases 1 and 7.

The results for Case 1 are shown in Fig. 11, where the horizontal axis represents the normalized distance from the cylinder center (*x*/*D*), and the vertical axis corresponds to the phase (*t*/*T*). The contour plots reveal that during 0.2<*t*/*T*<0.6, a positive peak in bed shear stress occurs within the region $-3<x/D<-1$. This observation aligns with the temporal and spatial activity of the horseshoe vortex discussed in the previous section. Thus, it can be seen that the vortex is compressed near the bed in this area, enhancing momentum transfer and exchange near the bed, and significantly amplifying the local bed shear stress upstream of the cylinder. The elevated shear stress imposes a stronger shear effect on the bed, which is expected to exacerbate erosion, sediment transport, and the associated scouring process. When *t*/*T*>0.6, due to the reversal of the flow direction, the bed shear stress exhibits an extreme negative value under the influence of the lee-wake vortex. The formation of the lee-wake vortex alters the flow structure, resulting in reverse momentum transfer in the region; this transfer inverts the direction of the bed shear stress. The negative shear stress exerts a shear effect opposite to the original direction, which may redistribute and redeposit sediment particles, altering the evolution and morphology of the scour.

The results for Case 7 are depicted in Fig. 12. Similar to Case 1, the positive and negative peaks in the

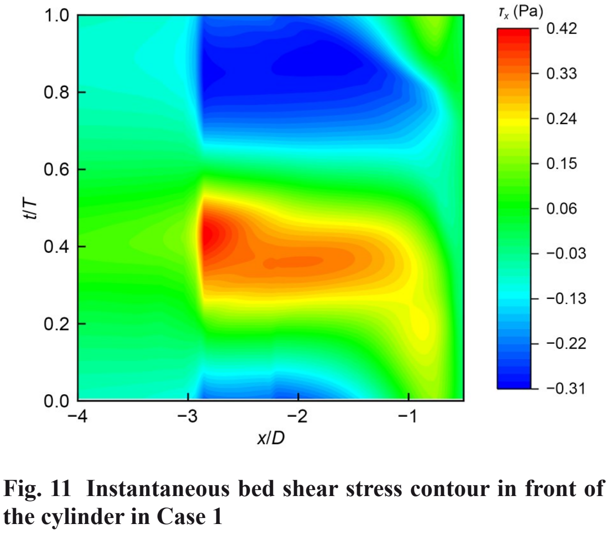

Fig. 11 Instantaneous bed shear stress contour in front of the cylinder in Case 1

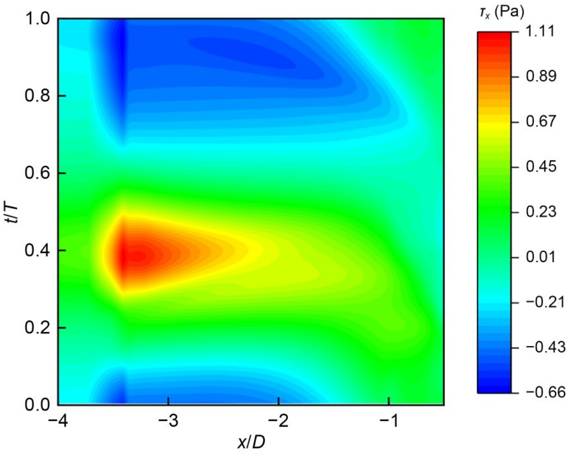

Fig. 12 Instantaneous bed shear stress contour in front of the cylinder in Case 7

bed shear stress correspond to the active periods of the upstream horseshoe vortex and the downstream lee-wake vortex development, respectively. Notably, in Case 7, the maximum positive shear stress reaches 1.11 Pa, representing a 164% increase compared to the 0.42 Pa observed in Case 1. Meanwhile, the maximum negative shear stress is −0.66 Pa, being 113% higher than Case 1. Differences between the two cases are evident in the spatial distribution of the shear stress peaks. In Case 7, the positive shear stress peak is farther from the cylinder compared to Case 1. This shift is consistent with the behavior illustrated in Figs. S4 and S5 in Section S3 of the ESM, where the upstream horseshoe vortex in Case 7 is located farther away from the cylinder than in Case 1. This shift in vortex position directly leads to a corresponding change in the position of the positive shear stress peak. Additionally, the negative shear stress peak in Case 7 has a broader spatial extent than in Case 1. This may stem from the large-scale vortex region near the bed (marked by the red rectangle in Fig. 6); this vortex region significantly influences the bed shear stress distribution, thereby expanding the spatial extent of the negative shear stress.

In 3D flow, the total bed shear stress can be characterized by the resultant of the shear stress components in the *x*- and *y*-directions (Wei et al., 2020), as:

$$\tau_{xy}=\sqrt{\tau_x^2+\tau_y^2}\,, \tag{6}$$

where τ_x is the bed shear stress component in the *x*-direction, and τ_y is the bed shear stress component in the *y*-direction.

The bed shear stress for Cases 1 and 7 is analyzed at two representative phases: *t*/*T*=0.40, corresponding to the active phase of the upstream horseshoe vortex, and *t*/*T*=0.84, corresponding to the active phase of the downstream horseshoe vortex. As shown in Fig. 13, in both cases the maximum bed shear stress occurs along the lateral sides of the upstream cylinder (marked by a black solid-line circle). This may be because as the flow passes around the cylinder, the narrowing flow path along the sides causes contraction of the streamlines and acceleration of the flow. The increased velocity in these regions sharply elevates the velocity gradient, resulting in peak shear stress. Furthermore, the extension of the horseshoe vortex along the cylinder's sides and into the downstream region further enhances the velocity gradient near the bed, amplifying the bed shear stress.

We also observe a region of reduced bed shear stress adjacent to the upstream surface of the cylinder (marked by a red solid-line rectangle). This reduction

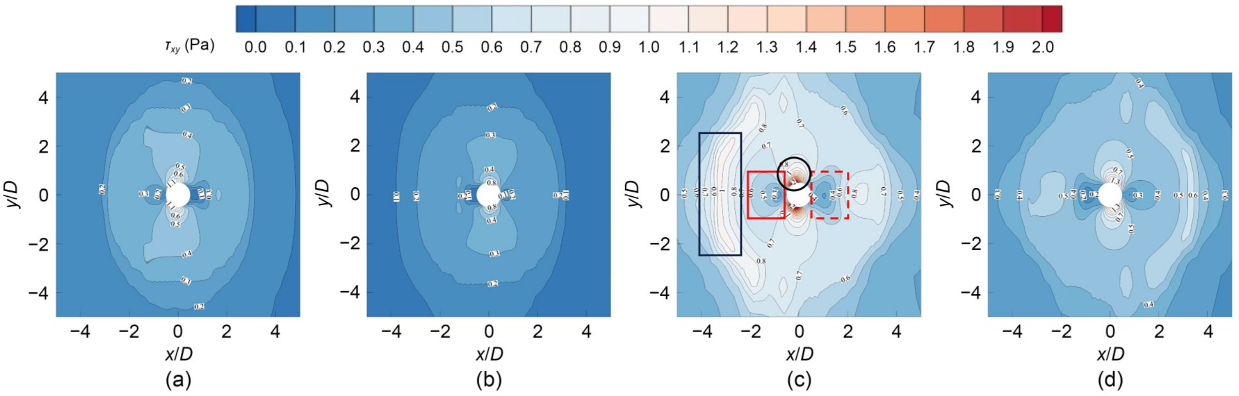

(a) (b) (c) (d)

Fig. 13 Instantaneous bed shear stress contour around the cylinder: (a) Case 1 at *t*/*T*=0.40; (b) Case 1 at *t*/*T*=0.84; (c) Case 7 at *t*/*T*=0.40; (d) Case 7 at *t*/*T*=0.84. References to color refer to the online version of this figure

in shear stress is likely due to the flow stagnation point which forms at the cylinder's leading edge as the flow impinges here directly. At the stagnation point, the flow velocity abruptly drops to zero (with kinetic energy being converted to pressure), significantly reducing the velocity gradient in this area. The high-pressure region at the cylinder's leading edge generates an adverse pressure gradient, meaning that pressure increases along the flow direction. This forces the flow to decelerate, further diminishing the velocity gradient near the bed and exacerbating the reduction in bed shear stress. The minimal shear stress upstream of the cylinder would promote sediment deposition (by forming a shallow scour region), while the accelerated flow around the sides increases shear stress, leading to a hole in the local scour. Similarly, next to the downstream surface of the cylinder, another region of reduced bed shear stress is identified (marked by a red dashed-line rectangle). This phenomenon may result from energy dissipation as the flow navigates around the cylinder. The cylinder acting as an obstruction causes a loss of kinetic energy in the downstream wake, resulting in lower overall flow velocities and reduced velocity gradients –these collectively affect the bed shear stress in this area.

At t/T=0.40, a horseshoe-shaped region of extreme bed shear stress (marked by a black solid-line rectangle) is observed in the range of $-4<x/D<-2$. This pattern might be a result of the active horseshoe vortex in this region, in which the vortex is compressed and tightly adheres to the bed, inducing intense rotation in the upstream flow field. The significant transfer and exchange of momentum near the bed significantly increases the bed shear stress. Such elevated shear stress would intensify sediment erosion and mobilization, which critically influences the scour process. At t/T=0.84, a similar peak bed shear stress region emerges downstream of the cylinder, as shown in Fig. 13d. However, the magnitude of bed shear stress in the downstream region is approximately 40% lower than in the upstream region.

The above results show that scour potential is not determined solely by an integral measure of vortex strength, but instead by the temporal sequencing and local topology of the flow features that concentrate momentum near the bed. Specifically, increasing KC shifts the timing of horseshoe vortex formation and increases the propensity of strong impinging jets and small-scale lee-side vortices to form during specific phases of the wave cycle. These localized jets and vortex impingements produce sharp, phase-dependent spikes in bed shear stress (orders of magnitude higher than the background values) which are highly relevant for short-duration sediment entrainment. Furthermore, the 3D Q criterion fields reveal that it is not just the in-plane vortex circulation, but also the vortex breakdown and rapid out-of-plane vorticity production that control the spatial extent of high-shear patches on the bed. Such observations explain why two cases with similar integrated vortex strength may nevertheless produce significantly different scour patterns—the phase and location at which momentum is focused onto the bed are crucial.

4 Conclusions

Numerical simulations were conducted to investigate the flow around a vertical cylinder under varying KC numbers.

At low KC numbers, the flow predominantly manifested as a single vortex structure. In contrast, high KC number cases showed coexistence of multiple vortices with significantly enhanced strength and a wider spatial extent. Compared with the upstream flow field, the downstream flow field maintained a relatively simpler structure, characterized by smaller-scale and weaker horseshoe vortices; moreover, dual-vortex coexistence was not observed.

Analysis of the dynamic pressure revealed a persistent negative pressure gradient along the cylinder surface, which promoted flow separation and propagation of horseshoe vortices. Notably, within the angular range of $35°<\varphi<180°$, a temporally evolving positive pressure gradient was identified, which intensifies separation between the boundary layers and fosters the formation of lee-wake vortices, ultimately influencing scour development patterns.

The 3D vortex structures identified by the Q criterion analysis revealed distinct evolutionary processes. At low KC numbers, the vortices demonstrated stable evolutionary patterns, while in high KC number cases, accelerated formation of the horseshoe vortex and prolonged vortex lifetimes were observed.

The distribution of bed shear stress was closely related to the activity of horseshoe vortices and lee-wake vortices. When upstream horseshoe vortices were active, the bed shear stress generated positive peaks near the cylinder. During the development of lee-wake vortices, the bed shear stress exhibited negative extremes, which may lead to the deposition and redistribution of sediment during scouring. Additionally, as the KC number increased, the overall bed shear stress near the cylinder substantially intensified, and the active region of the horseshoe vortices corresponded to a localized area of extreme bed shear stress.

Note that we used the RANS equations in the modeling, which due to their time-averaged nature, inadequately resolve small-scale turbulence and smooth out unsteady vortex details that are crucial for scour dynamics. To achieve higher-fidelity simulations, future work should prioritize using large eddy simulation (LES) or hybrid RANS-LES methods.

A promising direction for future study involves bridging the gap between the flow physics insights revealed by this work with practical engineering design. Subsequent research will explicitly correlate the simulated bed shear stresses with critical shear thresholds for sedimentation, and quantitatively evaluate the corresponding impact on scour depth evolution.

Acknowledgments

This work is supported by the "Leading Goose" R&D Program of Zhejiang Province (No. 2023C03122) and the Natural Science Foundation of Zhejiang Province, China (No. LY23E090003).

Author contributions

Ben HE: conceptualization, methodology, writing–review & editing, and resources. Junkang WENG: formal analysis, investigation, writing–original draft, and data curation. Yuan LIN: investigation, writing–original draft, and visualization. Yifan GAO: investigation and writing–original draft. Maoxing WEI: investigation and writing–review & editing. Fang HE: conceptualization, methodology, writing–review & editing, supervision, and funding acquisition.

Conflict of interest

Ben HE, Junkang WENG, Yuan LIN, Yifan GAO, Maoxing WEI, and Fang HE declare that they have no conflict of interest.

References

Apsilidis N, Diplas P, Dancey CL, et al., 2015. Time-resolved flow dynamics and Reynolds number effects at a wall–cylinder junction. *Journal of Fluid Mechanics*, 776:475-511.
https://doi.org/10.1017/jfm.2015.341

Baker CJ, 1980. The turbulent horseshoe vortex. *Journal of Wind Engineering and Industrial Aerodynamics*, 6(1-2):9-23.
https://doi.org/10.1016/0167-6105(80)90018-5

Bělík L, 1973. The secondary flow about circular cylinders mounted normal to a flat plate. *Aeronautical Quarterly*, 24(1):47-54.
https://doi.org/10.1017/S0001925900006417

Berger E, Wille R, 1972. Periodic flow phenomena. *Annual Review of Fluid Mechanics*, 4(1):313-340.
https://doi.org/10.1146/annurev.fl.04.010172.001525

Blondeaux P, 2012. Sediment mixtures, coastal bedforms and grain sorting phenomena: an overview of the theoretical analyses. *Advances in Water Resources*, 48:113-124.
https://doi.org/10.1016/j.advwatres.2012.02.004

Chanda A, Sarkar A, Bora SN, 2022. An analytical study of scattering of water waves by a surface-piercing bottom-mounted compound porous cylinder placed on a porous sea-bed. *Journal of Fluids and Structures*, 115:103764.
https://doi.org/10.1016/j.jfluidstructs.2022.103764

Chen QG, Qi ML, Zhong Q, et al., 2017. Experimental study on the multimodal dynamics of the turbulent horseshoe vortex system around a circular cylinder. *Physics of Fluids*, 29(1):015106.
https://doi.org/10.1063/1.4974523

Chen QG, Yang ZL, Wu HJ, 2019. Evolution of turbulent horseshoe vortex system in front of a vertical circular cylinder in open channel. *Water*, 11(10):2079.
https://doi.org/10.3390/w11102079

Choi J, Yoon SB, 2009. Numerical simulations using momentum source wave-maker applied to RANS equation model. *Coastal Engineering*, 56(10):1043-1060.
https://doi.org/10.1016/j.coastaleng.2009.06.009

Corvaro S, Marini F, Mancinelli A, et al., 2018. Hydro- and morpho-dynamics induced by a vertical slender pile under regular and random waves. *Journal of Waterway, Port, Coastal, and Ocean Engineering*, 144(6):04018018.
https://doi.org/10.1061/(asce)ww.1943-5460.0000470

Corvaro S, Crivellini A, Marini F, et al., 2019. Experimental and numerical analysis of the hydrodynamics around a vertical cylinder in waves. *Journal of Marine Science and Engineering*, 7(12):453.
https://doi.org/10.3390/jmse7120453

Dargahi B, 1989. The turbulent-flow field around a circular-cylinder. *Experiments in Fluids*, 8(1-2):1-12.
https://doi.org/10.1007/BF00203058

Devenport WJ, Simpson RL, 1990. Time-depeiident and time-averaged turbulence structure near the nose of a wing-body junction. *Journal of Fluid Mechanics*, 210:23-55.
https://doi.org/10.1017/S0022112090001215

Gao Q, Ortiz-Dueñas C, Longmire EK, 2011. Analysis of vortex populations in turbulent wall-bounded flows. *Journal of Fluid Mechanics*, 678:87-123.
https://doi.org/10.1017/jfm.2011.101

Guan DW, Xie YX, Chiew YM, et al., 2024. Estimation of local scour around monopile foundations for offshore structures using machine learning models. *Ocean Engineering*, 296:116951.
https://doi.org/10.1016/j.oceaneng.2024.116951

He F, Weng JK, Lin Y, et al., 2024. Investigating the characteristics of horseshoe vortex around a vertical circular cylinder in waves using particle image velocimetry: an experimental study. *Physics of Fluids*, 36(8):085142.
https://doi.org/10.1063/5.0215043

Jang HK, Ozdemir CE, Liang JH, et al., 2021. Oscillatory flow around a vertical wall-mounted cylinder: flow pattern details. *Physics of Fluids*, 33(2):025114.
https://doi.org/10.1063/5.0032643

Kolář V, 2010. A note on integral vortex strength. *Journal of Hydrology and Hydromechanics*, 58(1):23-28.
https://doi.org/10.2478/v10098-010-0003-3

Laursen EM, Toch A, 1956. Scour Around Bridge Piers and Abutments. Iowa Highway Research Board, USA.

Li JZ, Qi ML, Fuhrman DR, et al., 2018. Influence of turbulent horseshoe vortex and associated bed shear stress on sediment transport in front of a cylinder. *Experimental Thermal and Fluid Science*, 97:444-457.
https://doi.org/10.1016/j.expthermflusci.2018.05.008

Miozzi M, Corvaro S, Pereira FA, et al., 2019. Wave-induced morphodynamics and sediment transport around a slender vertical cylinder. *Advances in Water Resources*, 129:263-280.
https://doi.org/10.1016/j.advwatres.2018.01.025

Pierce FJ, Harsh MD, 1988. The mean flow structure around and within a turbulent junction or horseshoe vortex—Part II. The separated and junction vortex flow. *Journal of Fluids Engineering*, 110(4):415-423.
https://doi.org/10.1115/1.3243572

Qi WG, Gao FP, 2014. Equilibrium scour depth at offshore monopile foundation in combined waves and current. *Science China Technological Sciences*, 57(5):1030-1039.
https://doi.org/10.1007/s11431-014-5538-9

Qi WG, Li YX, Xu K, et al., 2019. Physical modelling of local scour at twin piles under combined waves and current. *Coastal Engineering*, 143:63-75.
https://doi.org/10.1016/j.coastaleng.2018.10.009

Qi WG, Liu J, Gao FP, et al., 2022. Quantifying the spatiotemporal evolution of the turbulent horseshoe vortex in front of a vertical cylinder. *Physics of Fluids*, 34(1):015110.
https://doi.org/10.1063/5.0076648

Sarkar A, Chanda A, 2022. Structural performance of a submerged bottom-mounted compound porous cylinder on the water wave interaction in the presence of a porous sea-bed. *Physics of Fluids*, 34(9):092113.
https://doi.org/10.1063/5.0106425

Schanderl W, Manhart M, 2016. Reliability of wall shear stress estimations of the flow around a wall-mounted cylinder. *Computers & Fluids*, 128:16-29.
https://doi.org/10.1016/j.compfluid.2016.01.002

Schanderl W, Jenssen U, Strobl C, et al., 2017. The structure and budget of turbulent kinetic energy in front of a wall-mounted cylinder. *Journal of Fluid Mechanics*, 827:285-321.
https://doi.org/10.1017/jfm.2017.486

Sumer BM, Fredsøe J, Christiansen N, 1992. Scour around vertical pile in waves. *Journal of Waterway, Port, Coastal, and Ocean Engineering*, 118(1):15-31.
https://doi.org/10.1061/(asce)0733-950X(1992)118:1(15)

Sumer BM, Christiansen N, Fredsøe J, 1997. The horseshoe vortex and vortex shedding around a vertical wall-mounted cylinder exposed to waves. *Journal of Fluid Mechanics*, 332:41-70.
https://doi.org/10.1017/S0022112096003898

Wei MX, Chiew YM, Cheng NS, 2020. Particle image velocimetry measurements of bed-shear stress induced by wall-bounded swirling jets. *Journal of Engineering Mechanics*, 146(6):04020052.
https://doi.org/10.1061/(asce)em.1943-7889.0001781

Zhou J, Adrian RJ, Balachandar S, et al., 1999. Mechanisms for generating coherent packets of hairpin vortices in channel flow. *Journal of Fluid Mechanics*, 387:353-396.
https://doi.org/10.1017/S002211209900467X

Electronic supplementary materials

Sections S1–S3